Additive Manufacturing 21 (2018) 17–29

Contents lists available at ScienceDirect

Additive Manufacturing

journal homepage: www.elsevier.com/locate/addma

Full Length Article

Effect of size, morphology, and synthesis method on the thermal and sintering properties of copper nanoparticles for use in microscale additive manufacturing processes

Nilabh K. Roy[a], Chee S. Foong[b], Michael A. Cullinan[a,*]

[a] Department of Mechanical Engineering, The University of Texas at Austin, Austin, TX, 78712, USA
[b] NXP Semiconductors Austin, TX, 78735, USA

ARTICLE INFO

Keywords:
Copper nanoparticles
Micro-scale selective laser sintering
Additive manufacturing
Surface coatings
Physical and thermal characterization

ABSTRACT

Additive manufacturing using nanoparticles (NPs) is a growing field due to the ever-increasing demand for parts with smaller and smaller features. Of particular interest are copper nanoparticles (Cu NPs) due to the ubiquitous use of Cu in microelectronics applications. There are numerous methods currently available to synthesize Cu NPs in both powder and ink forms. However, the effect of how the NPs are manufactured on the sintering properties of the NPs produced is not well understood. This paper shows that NP size, morphology, and synthesis method can have a significant effect on the sintering temperature and sintering quality for Cu NPs. In addition, surface coatings and surfactants used in Cu NP inks can help to reduce agglomeration in the dried NP samples, prevent oxidation of the Cu NPs, and restrict the sintering of the Cu NPs at lower temperatures due to the need to thermally remove the surface coatings before sintering can occur. Therefore, these coatings improve the Cu NP packing density and increase the temperature required for necking to occur which leads to better sintering of the Cu NP ink samples. It is also observed in this paper that most of these surface coatings are removed during the sintering processes leaving the sintered parts with a much higher Cu percentage than contained in the original NPs. However, at temperatures near the melting temperature of the Cu NPs, the surface coatings can start to graphitize and hinder the fusion of the NPs. Therefore, the optimal sintering conditions for Cu NP inks are at temperature high enough to break down the polymer surface coating on the NPs but low enough that the Cu NPs do not start to melt and that graphitizing of the surface coatings does not start to occur.

1. Introduction

In most commercial sintering applications, powders with particle size on the order of tens of microns are used as raw materials and do not require an extensive study of the material properties as their properties are similar to the bulk properties of the material. However, as the size of particles decreases to less than a micron, the divide between the bulk material properties and nanoparticles' (NPs') properties becomes wider and many new phenomena are encountered too. Thus, to achieve good quality sintered parts using NPs, it is important to have an understanding about the different phenomena that are specific to only NPs like agglomeration of NPs, melting point depression, early onset of sintering and so on. This study was primarily directed towards that objective i.e. to determine the effect of size, morphology, surface coating and synthesis methods on the physical, chemical and thermal changes that these particles undergo while being heated during the sintering reaction.

Metal selective laser sintering (SLS) is an additive manufacturing technology that uses a high-power laser to locally heat and fuse metal particles together into a mass that has a desired three-dimensional shape. In this process, the metal powders are initially spread into a thin layer to form a metal powder bed. The laser then selectively scans the powder bed and fuses the metal powders on the surface of the powder bed together at selected locations based on a previously generated CAD file. After one layer of the metal powder is sintered, the powder bed is lowered by one layer thickness. Another layer of the metal powder is spread onto the powder bed creating a new metal layer that can be scanned and sintered. The process is repeated until an entire three dimensional part is built up [1,2]. The smallest feature sizes that commercially available sintering machines can currently typically achieve are on the order of hundreds of microns due in part to the microscale powders typically used in the sintering operation. To produce parts with finer feature sizes, the use of nanoscale powders will be required. Therefore, this study is focused towards analyzing the thermal and

* Corresponding author.
E-mail address: michael.cullinan@austin.utexas.edu (M.A. Cullinan).

https://doi.org/10.1016/j.addma.2018.02.008
Received 22 September 2017; Received in revised form 18 February 2018; Accepted 21 February 2018
Available online 02 March 2018

physical properties of nanopowders within the powder bed of a microscale selective laser sintering (μ-SLS) system that is designed to be able to achieve 1 μm feature sizes [3,4]. The primary application for the μ-SLS system is microelectronics packaging including the fabrication of solder bumps and 3D interconnect structures [3]. Hence, Cu has been chosen as the material to study because of its wide application as interconnection metal in integrated circuits due to its good electrical conductivity and lower cost compared to silver and gold. Also, Cu lines show at least a 40% reduction in resistance for interconnects as compared to aluminum lines and hence decreases the time constant product (RC) value which reduces the interconnect delay and enhances the performance of the chip [5].

To get feature sizes of 1 μm, it is required to use particles at least an order of magnitude smaller than the feature size and hence, NP based powders are used within the μ-SLS system. However, NPs have their own limitations including excessive agglomeration and oxidation. Nanoscale powders possess high surface energies and, therefore, tend to agglomerate in order to reduce the surface energy of the system. Also, since NPs have a high surface area-to-volume ratio, oxidation becomes unavoidable in contact with air and thus, a high vacuum is sometimes required for sintering the nanoscale powders. In addition, van der Waals forces dominate over gravitational forces at the nanoscale which changes the sintering properties of the NPs. It is because of these reasons that the properties of these NPs are significantly different from the bulk properties of the microscale powders [2,6]. Therefore, a thorough analysis of the physical, thermal, and sintering properties of these NPs is required to accurately model the heat transfer that occurs within the NP-based powder bed during the sintering operation and to be able to estimate the power requirements for sintering depending upon the spot size and layer thickness. This analysis is critical in being able to optimize the microscale selective laser sintering process to produce high quality, micron scale features.

Seven samples of Cu NPs were tested for this study. Four of these NPs were received in powder form and the rest of them were received in ink form. These tests were done to comprehensively characterize the different NPs produced by different techniques such as electric explosion of wire, laser ablation synthesis, chemical reduction, and other chemical synthesis methods. The different coatings on these NPs including passive oxide layer, carbon coating, and polyvinylpyrrolidone (PVP) coating also affect the properties of these NPs and hence, the need for these studies to identify the best candidate for use in μ-SLS systems. Certain desirable properties which are sought in the NPs included an average particle size of less than 100 nm with the largest particles not being greater than 200 nm to achieve 1 μm resolution on the final part, low agglomeration tendencies, low levels of impurities so that the sintering process is uniform, low oxidation, and a morphology of the particles that is spherical or close to spherical to improve the specific heat capacity and thus, reducing the total energy required by the particles to sinter [7].

2. Background

The morphology of particles i.e. the shape, size and distribution of particles has been shown and widely reported to affect the mechanical properties of additively manufactured parts. Smaller particle sizes have been shown leading to increased particle packing efficiency in the bed which in turn leads to density closer to the bulk material density and lower surface roughness [8,9]. However, as the particle sizes are reduced, they tend to agglomerate in powder samples. The presence of agglomerates in the bed has been found to negatively affect the flow behavior [10], increased balling up of particles [11], increased porosity and thus lower part density. Similarly, samples with irregular shaped particles have been shown to have higher interparticle friction compared to samples with spherical particles. This higher interparticle friction severely degrades the flow behavior leading to poor layer densities [12]. Since these morphological properties of particles are directly linked to their synthesis process, the synthesis method plays a pivotal role in determining the final properties of the AM part. In addition to the morphological properties, the microstructure and phase evolution of particles and ultimately that of the final part is also highly dependent on the synthesis method as shown by Rafi et al. [13] and corroborated by Slotwinski et al. [14] that the microstructure of the final part depended primarily on the microstructure of the parent powder which was affected by the gas used for atomization in their synthesis process. The variation in microstructure evolution of nanoparticles depending on the synthesis parameters has been an interesting area of study for researchers [15,16] and can be useful in explaining the properties of the final part.

Many different methods are commonly used for the synthesis of Cu NPs and these methods can be characterized into the following categories: 1) chemical synthesis methods, 2) physical synthesis methods, and 3) biological synthesis methods [17]. The common chemical synthesis methods include chemical reduction [18], sono-chemical reduction [19], hydrothermal assisted [20], electrochemical [21], and micro-emulsion assisted techniques [22]. Laser ablation synthesis [23], electric explosion of wire [24], vacuum vapor deposition [25] and mechanical milling [26,27] are some of the more commonly used physical methods. Biosynthesis of NPs primarily involves oxidation/reduction as the main reaction during the production. In biosynthesis methods, metal compounds are usually reduced into their respective NPs by microbial enzymes or by plant phytochemicals with antioxidant or reducing properties [17,28]. In addition, Cu NPs are often coated with protective polymers [29,30] or surfactants [31–33] to prevent their oxidation and agglomeration. Usually, chemical synthesis methods are more effective than physical synthesis at producing uniform NPs because chemical synthesis methods provide better control over the size and morphology of the particles that are produced than the physical methods.

Some of the most commonly used techniques for mass production of NPs are chemical reduction, laser ablation synthesis and electric explosion of wire (EEW). In the chemical reduction techniques, a copper salt is reduced by a reducing agent such as sodium borohydride, hydrazine (N_2H_4), ascorbate, polyol, isopropyl alcohol with cetyltrimethylammonium bromide (CTAB), while glucose is used as the stabilizing agent [30,34]. Laser ablation is a commonly used technique for the preparation of Cu NPs in colloidal form in a variety of solvents [35]. Factors that affect the final NPs produce by laser ablation are the type of laser, number of pulses, pulsing time, and type of solvent used in the ablation process. Electric explosion of Cu wires is also used in the production of Cu NPs. In this method, high-voltage (15–30 kV) and powerful (density 10^{11}–10^{12} A/m^2) impulse (duration 10^{-4}–10^{-7} s) flows through the wire causing it to explode into NPs [36]. In EEW low electric densities, E/E_S = 0.8–1.5 where E is the comparative explosion energy and E_S is the sublimation energy of exploded material, are typically used. The limitation of EEW as a method of NPs production lies in a great dispersion of particle diameters (nanometers to 10′s of micrometers) produced by this method [24]. The Cu samples that are presented in this study have been prepared by using chemical reduction, electric explosion of wire, and laser ablation synthesis methods. This paper presents a comparative study of the physical and thermal properties of Cu NPs produced by different methods and for μ-SLS applications.

3. Experimental setup and results

3.1. Effect of synthesis method on the morphology of Cu NPs produced

In order to physically characterize the Cu NPs created using different synthesis methods, Scanning Electron Microscopy (SEM) was used to measure the particle size and morphology of the NPs. Both size and morphology of particles are important to achieve good quality sintered parts with the desired micron scale feature size. These SEM

Table 1
Description of Cu NP samples used in the study.

Sample Number	Sample Description with Nominal Particle Size	Measured Particle Size (nm)	Measured Sintering Temperature	Production Method	Unsintered NP Morphology	Coating Layer
1	40 nm Cu NPs (USRN, Inc)	20–400	230 °C	Electric Explosion of Wire	Spherical, Agglomerated	None
2	100 nm Cu NPs (USRN, Inc)	40–300	242 °C	Electric Explosion of Wire	Irregular, Agglomerated	None
3	25 nm Carbon Coated NPs (USRN, Inc)	20–340	322 °C	Laser Ablation	Irregular, Agglomerated and Highly Fibrous	Carbon
4	25 nm Passivated Cu NPs (MKNano)	40–670	275 °C	Laser Ablation	Spherical, Agglomerated	Copper Oxide
5	100 nm Cu ink (Applied Nanotech, Inc)	20–170	330 °C	Chemical Synthesis	Spherical	Carbon
6	90 nm Cu ink for Glass Substrate (Intrinsiq Materials, Inc)	10–210	416 °C	Chemical Synthesis	Spherical	PVP
7	90 nm Cu ink for Polyimide Substrate (Intrinsiq Materials, Inc)	30–220	420 °C	Chemical Synthesis	Spherical	PVP

images were also used to analyze the extent of agglomeration in the sample. Differential scanning calorimetry was used to analyze the sintering properties of the Cu NPs as discussed in Section 3.3. Manufacturer details along-with average particle size as provided by the manufacturer, production method and coating description for different Cu NPs used in this study are given in Table 1. Table 1 also includes the measured particles sizes and measured sintering temperature found for each of the NP samples tested.

Figs. 1 and 2, show two samples prepared by electric explosion of wire with different average particle sizes, 40 nm and 100 nm respectively. Figs. 1a) and 2a) show the extent of agglomeration in these samples. As these samples were prepared by a physical explosion process, they do not have any coating to prevent any agglomeration. Some of the agglomerates were found to be as big as 120 µm. Secondly, the range of the individual particle size was 20–400 nm and 40–300 nm for the two samples with average particle size (APS) 40 nm and 100 nm respectively. The particles with APS of 100 nm were found to be mostly irregular in shape which is undesirable because it creates larger voids in the initial particle packing and hinders good sintering of the NPs. Controlling the size of NPs using EEW is difficult [24] as the particles obtained have a very wide size distribution. Therefore, NPs synthesized by EEW are generally not well suited for microscale additive manufacturing processes.

Figs. 3 and 4 show the Cu NPs samples obtained by laser ablation. Both these samples had a protective coating (either a thin oxide layer (2–4 nm) or a carbon coating) to prevent them from further oxidation and agglomeration. As discussed before, both these properties make them desirable for sintering applications, however each of them had their own limitations. Although the 25 nm passivated particles are spherical in shape (Fig. 3b), their size distribution is very wide with some particles being as big as 650 nm which may prove a hindrance in achieving 1 µm features and will also affect the packing density of the powder bed. On the other hand, 25 nm carbon coated sample was fibrous in appearance and also had highly agglomerated particles as seen in their SEM micrographs.

The SEM images of all the dry powders show significant agglomeration of NPs in the sample. In fact, individual NPs in these samples can agglomerate into particles that can be up to a few hundred microns in diameter. This agglomeration of the dry NPs is due to the fact that high surface area to volume ratio of individual NPs results in a very high surface energy for NPs and in order to minimize the surface energy of the powder bed, the NPs agglomerate into larger particles. This uncontrolled agglomeration of NPs is driven by the attractive van der Waals forces between particles [37]. In addition to the agglomeration, the fact that spreading dry nanopowders to achieve the packing density for good quality sintered part is very difficult, NP inks were tested. Cu NP inks can be easily spread over a substrate with very good packing density using methods like spin coating and slot die coating.

Fig. 5 shows the SEM images of the spin coated 100 nm Cu ink on aluminum substrate. The ink was spin coated at 1000 rpm for 60 s and then dried at 85 °C for 15 min. The particles appear more uniform in size compared to powder samples. Also, the extent of agglomeration is much lower than that of the powders due to the use of surfactants and dispersants in the NP inks. Figs. 6 and 7 show similar spin coated samples for 90 nm Cu NP inks designed for polyimide and glass substrates.

All the three inks imaged under the SEM showed similar morphologies, packing densities, and size distributions. The reason that the particles in the ink do not agglomerate is due to the presence of a stabilizing agent which is used in the chemical synthesis of these inks. Polyvinylpyrrolidone (PVP) was the stabilizing agent used in the production of 90 nm Cu inks for both glass and polyimide substrate. Based on these SEM images, the three inks have better morphology, narrow size distribution, and lower agglomeration compared to all the powders

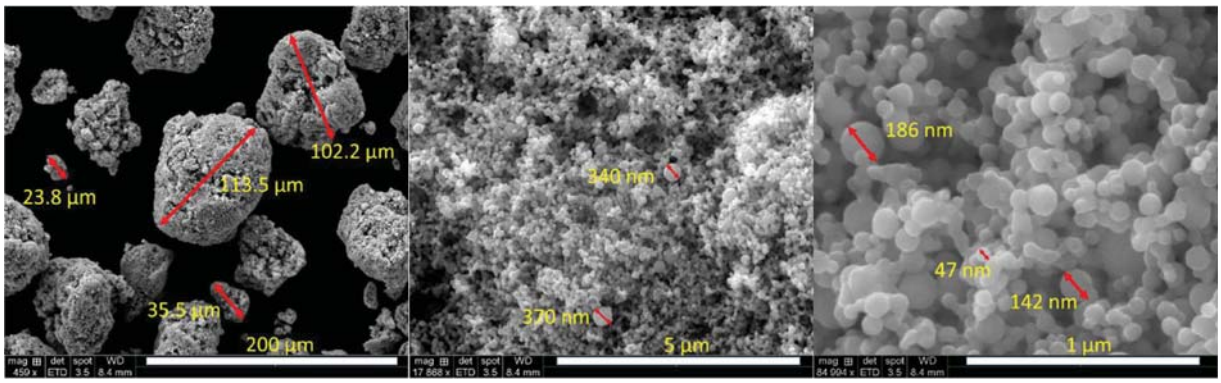

Fig. 1. SEM micrographs of 40 nm Cu NPs showing a) agglomeration in the sample b) & c) extent of particle sizes in the sample.

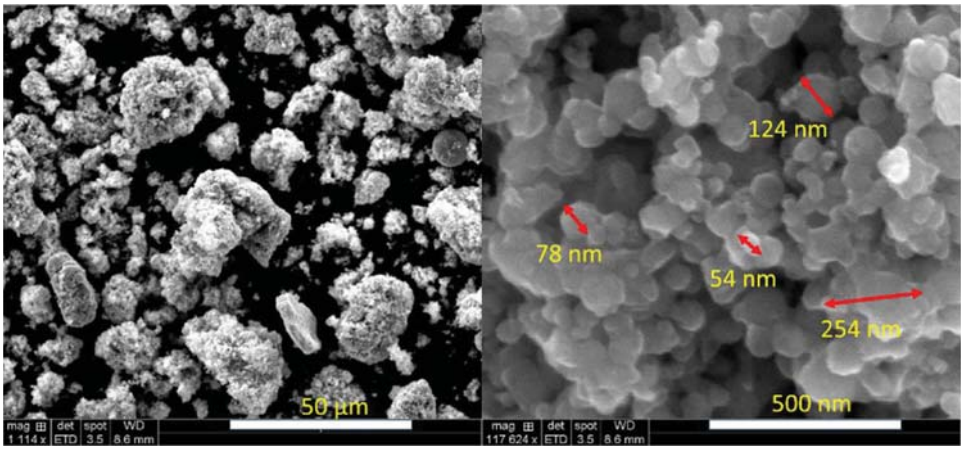

Fig. 2. SEM micrographs of 100 nm Cu NPs a) showing agglomeration b) irregular shape and wide range of particle size in the sample.

that were tested. Apart from the size, morphology, and agglomeration extent of the samples, the powders were also characterized based on their skeletal density. The skeletal density of different powders varied between 81% and 90% of the density of bulk Cu when measured using He Pycnometry (See Supplementary Table S1 for the data). This reduction in density compared to the bulk Cu could be attributed to the presence of foreign elements like carbon and oxygen in the samples. An analysis of these impurities is presented in the next section.

3.2. Effect of synthesis method on initial chemical composition of Cu NPs

Energy Dispersive X-Ray (EDX) Spectroscopy [38] was performed to detect the impurities or foreign elements in the Cu NPs leading to a reduction in the skeletal density as reported above. EDX is a good first-hand technique to estimate the composition of a sample. The experiment was carried out using FEI Quanta 650 SEM/ESEM and the data obtained was ZAF corrected.

For Cu nanopowder samples (Fig. 8), the weight percentage of Cu varied between 75% and 88%. All the samples had significant oxygen content suggesting that the samples had partially oxidized by the time tests were run. As expected, a higher carbon concentration was observed for the 25 nm carbon coated Cu NP sample. Presence of carbon in other samples could be attributed to the formation of adventitious carbon layer on being exposed to air. 40 nm Cu sample had the highest Cu content amongst the powder samples and hence, the best choice among the powders for further analysis.

All the three inks showed similar composition with Cu concentration varying between 75% and 81%, carbon concentration between 13% and 16.5% and oxygen concentration between 6% and 8% (Fig. 9). As expected, the carbon concentration in the inks was higher compared to the powders as the inks are dispersed in organic solvents and some of that residual solvent is left in the sample even after drying the sample. However, it is the organic dispersants which also prevent the particles from oxidizing and that was validated by the lower oxygen concentration in the inks as compared to the powders. Though 90 nm Cu inks were expected to show nitrogen peaks, nitrogen has only one peak of weak energy (392 eV) and it requires an accelerating voltage of only 1 KV to detect the nitrogen accurately. But with elements like Cu in the sample whose K_α line is at 8.04 keV, the accelerating voltage had to be maintained at 20 KV to capture the Cu concentration in the sample. With such high accelerating voltages, it is almost impossible to detect small quantities of nitrogen in the sample.

The results on particle size range, morphology, and composition of the particles for different Cu NP samples are summarized in Table 1. Overall, the powders display a larger variation in size of particles as compared to the ink samples suggesting that the chemical methods for preparation of NPs provide a better control over the size of NPs. Controlling the size of NPs is important for applications which aim to build parts with micron size features. Also, all the powder samples (including the ones with protective coatings) were significantly oxidized and agglomerated as observed from the EDX data. These problems were also significantly reduced in the ink samples where the extent of agglomeration was much lower and oxygen content was also lower than that of the powder samples. As discussed before, these are two of the characteristics that make a sample desirable for sintering. Lower agglomeration facilitates easier spreadability of raw material, enhances

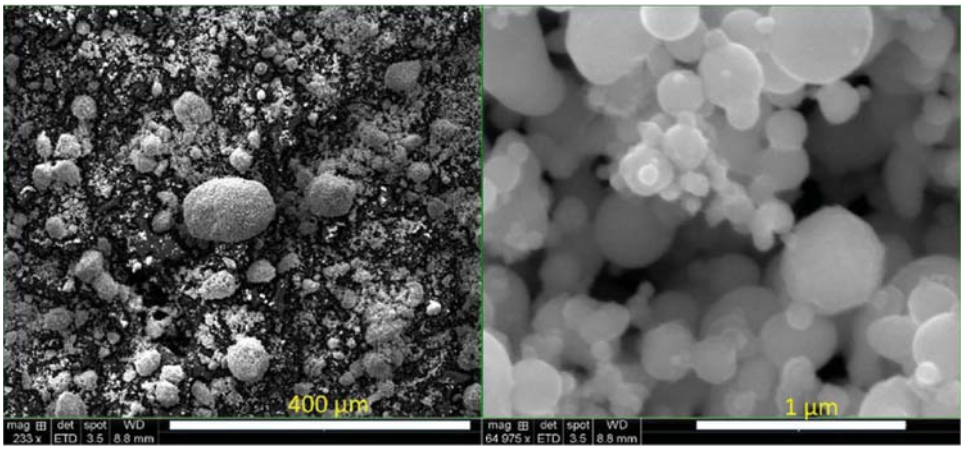

Fig. 3. a) and b). SEM micrographs of 25 nm passivated Cu NPs.

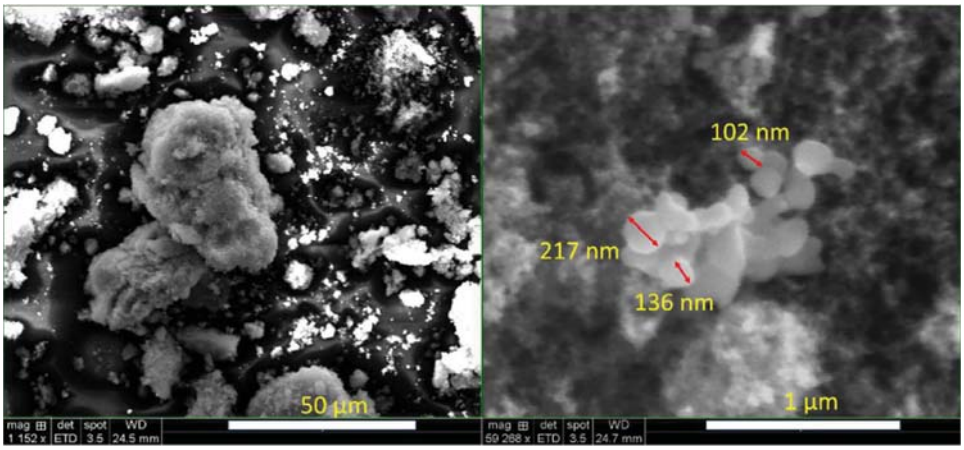

Fig. 4. a) and b). SEM micrographs of 25 nm carbon coated Cu NPs.

packing efficiency in the bed while a sample with high Cu content produces parts with properties close to bulk Cu. Both these characteristics helps to produces parts with better mechanical and electrical properties. Uniformly spherical morphology of particles makes the heat transfer process more effective by reducing the specific heat capacity and thus reducing the energy requirements of the setup [7,39]. Therefore, Cu NP inks are likely a better choice for microscale additive manufacturing processes but the sintering of these particles must still be analyzed in order to make a definitive conclusion.

3.3. Effect of synthesis method on sintering temperature and sintering quality

Differential Scanning Calorimetry (DSC) was employed to obtain the thermal profile of the NP sintering and to observe any physical or chemical changes that the NPs undergo while heating the sample. Although, bulk Cu has a melting temperature, T_m of 1085 °C, the melting temperature of nano-sized Cu particles can be much lower [40] and thus there is a need to study the thermal changes that Cu NPs undergo while heating. X-ray photoelectron spectroscopy (XPS) of the samples was carried out for samples heated to different temperatures to analyze the elemental composition and chemical bonding states of materials. DSC of the samples was carried out using Mettler- Toledo TGA/DSC Star 1e system which serves dual purpose that is it performs both thermogravimetric analysis (TGA) and DSC analysis simultaneously. Alumina crucibles (70 µl, annealed at 1100 °C, max. operating temperature −2000 °C) were covered with lid to prevent any oxidation of the sample at higher temperatures. The sample was heated at a rate of 10 °C/min from 40 °C to 1085 °C and nitrogen was used as the purge gas for the experiment with a flow rate of 50 ml/min. XPS of the samples was performed using Kratos X-Ray Photoelectron Spectrometer- Axis Ultra DLD and SEM images were taken using Hitachi S5500 SEM while some were taken using FEI Quanta 650 SEM/ESEM.

Figs. 10 and 11 show the thermal profiles for different samples when they were heated from 40 °C to 1085 °C. All powder samples show exothermic peaks in the temperature range 200 °C–350 °C. On the other hand, the 100 nm Cu ink shows an exothermic peak at 330 °C while the other two inks show endothermic peaks at 420 °C. The temperatures where the peaks and valleys occur have been summarized in Table 1. The peaks for the powder samples lie between 215 and 275 °C except for 25 nm-carbon coated sample which has a peak at 322 °C. These peaks are also accompanied by a loss in weight of the sample indicating that the surface coatings or surfactants that may be present on the NPs are starting to get removed at these temperatures. Fig. 13 shows peaks in respective derivative mass loss curve for the powder samples between 150 °C and 250 °C for the powders with the exception of carbon coated powders which shows two peaks: one at 338 °C and the other one at 472 °C. For the 100 nm Cu ink, an exothermic peak was observed accompanied by a high weight loss at 330 °C. These exothermic peaks in the DSC curves could be attributed to the onset of surface sintering reaction [41]. During the surface sintering reaction, the diffusion between the unstable atoms on the surface leads to the generation of heat. During this reaction, stabilization of the crystal structure, reformation, and reallocation of grain boundaries at the particle/particle interface can occur. Due to a very high surface area and highly defective surface, the surface energies of the NPs are very high which makes the atoms on

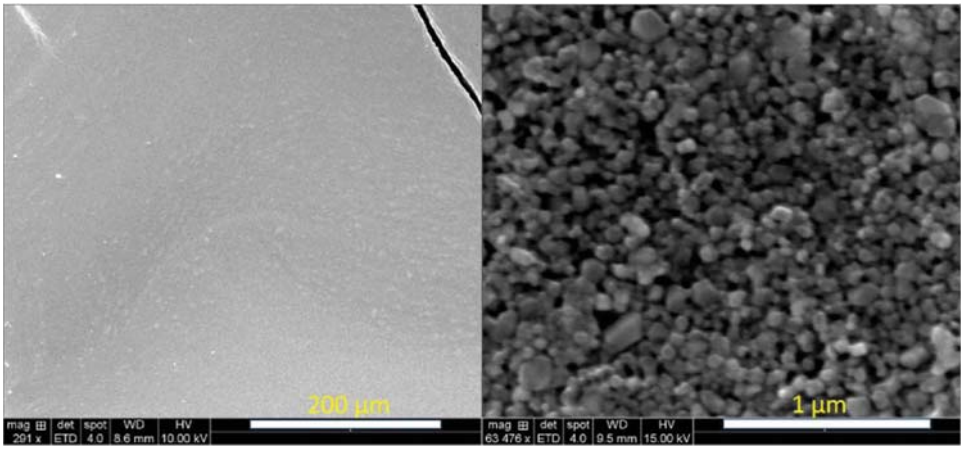

Fig. 5. a) and b). SEM micrographs of 100 nm Cu ink.

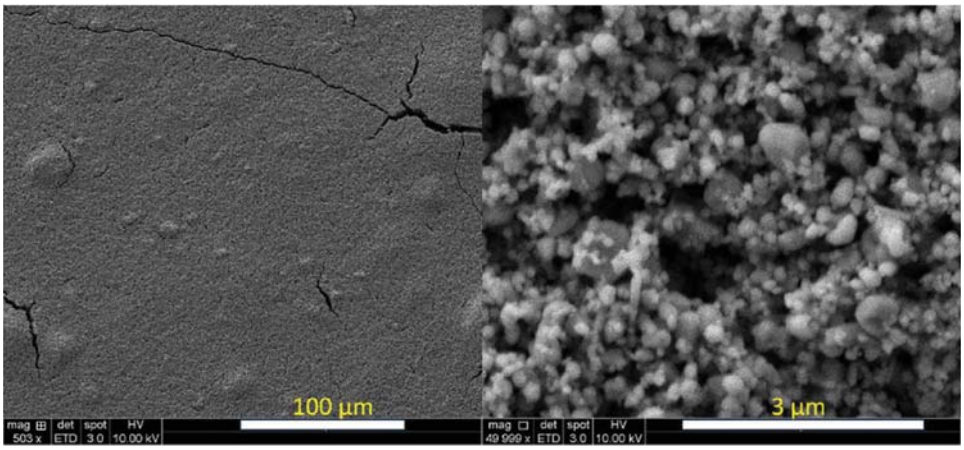

Fig. 6. a) and b) SEM micrographs of 90 nm Cu ink for polyimide substrate.

the surface very active. For this reason, surface sintering or melting of NPs occurs at a lower temperature than that of the bulk materials. Therefore, exothermic reaction that was found in DSC is likely due to surface sintering occurring at around 330 °C [41]. Creation of gas phases from the vaporization of organics from the NP surface could be another source of the exothermic peak which would help to explain the weight loss observed at this temperature by the TGA. The other two 90 nm Cu inks had exothermic peaks at 186–190 °C followed by endothermic peaks at 416–420 °C. For the 90 nm Cu inks, these exothermic peaks are believed to be caused by removal of moisture and residual organic solvents. Both these inks had a protective PVP coating layer which has been found to decompose at temperatures ranging from 350 to 450 °C [42]. As the PVP layer is decomposed, the surface sintering phenomenon among the NPs is initiated and continues till the melting point as is depicted by the continually rising exothermic peaks of these inks.

The weight loss during heating was monitored using TGA, as shown in Figs. 12 and 13. The powder samples showed weight loss at two regions, one around 130 °C–150 °C and the other around 200 °C–250 °C. Weight loss at lower temperatures likely arose from removal of moisture adsorbed on the particle surface while the weight loss at higher temperatures (200–250 °C) could be attributed to evaporation or de-bonding of organic surfactants from the surface of NPs. The weight loss for the powders was around 2–4% during the whole heating cycle except for the 25 nm-carbon coated sample. The carbon coated sample showed derivative mass loss peaks at 338 °C and 472 °C. The two separate peaks suggest that the onset of surface sintering and removal of carbon coating occur at different temperatures and this is validated by the thermal profile of the carbon coated sample where the heat flow peaks can be seen at the same temperatures −324 °C and 462 °C. Also, the weight loss was significantly higher compared to the other powder samples (13% as compared to 4%) indicating the removal of the thicker surface coating. As can be seen from the SEM images in Figs. 14 and 15, the NPs in the 40 nm Cu powder seem to have started to fuse together to form necks at around 260 °C and have completely fused to form a solid part by the time they reach the melting temperature.

For the ink samples, the derivative mass loss peaks match well with the heat flow peaks. The derivative mass loss peaks were also higher for the inks than any of the powders and the overall weight loss (14%–18%) for the inks was also higher compared to the powders. A possible explanation is that the residual organic solvent left in the dried ink could not be removed in the drying process and is removed only when heated to higher temperatures. 90 nm Cu ink samples had two inflexion points (first at 190 °C and the second at 410–420 °C) against one inflexion point for 100 nm Cu ink at 320–330 °C again indicating a two-stage sintering process for the 90 nm Cu ink samples where the solvent and PVP coatings are removed at two different temperatures. It is interesting to note that almost the entire weight loss for 100 nm ink samples is completed by 400–425 °C while that of the inks with PVP coating continues until the melting point. Even the heat flow rate curve for the 100 nm Cu ink sample stabilizes by 400 °C while that of the other two inks keep rising till the melting point indicating that the surface sintering of 100 nm Cu ink is completed at much lower temperatures and no significant changes take place after that. On the other hand, surface sintering of the PVP coated ink sample continues till the melting point.

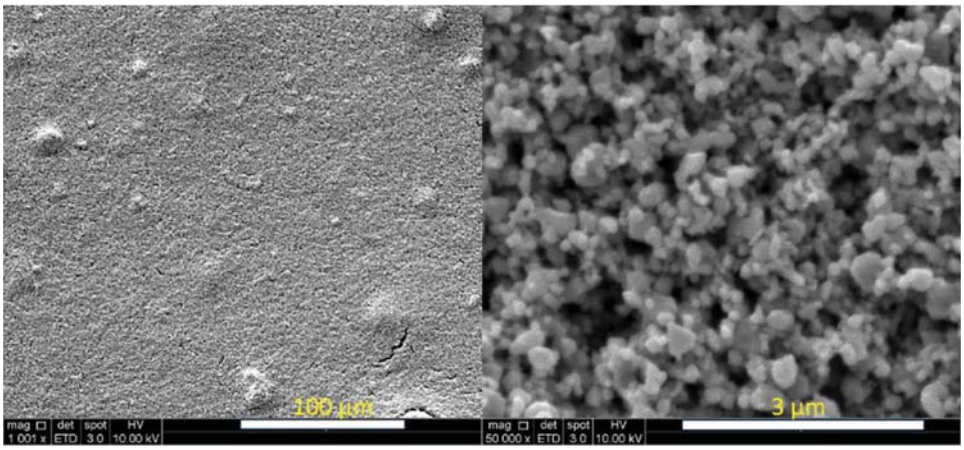

Fig. 7. a) and b) SEM micrographs of 90 nm Cu ink for glass substrate.

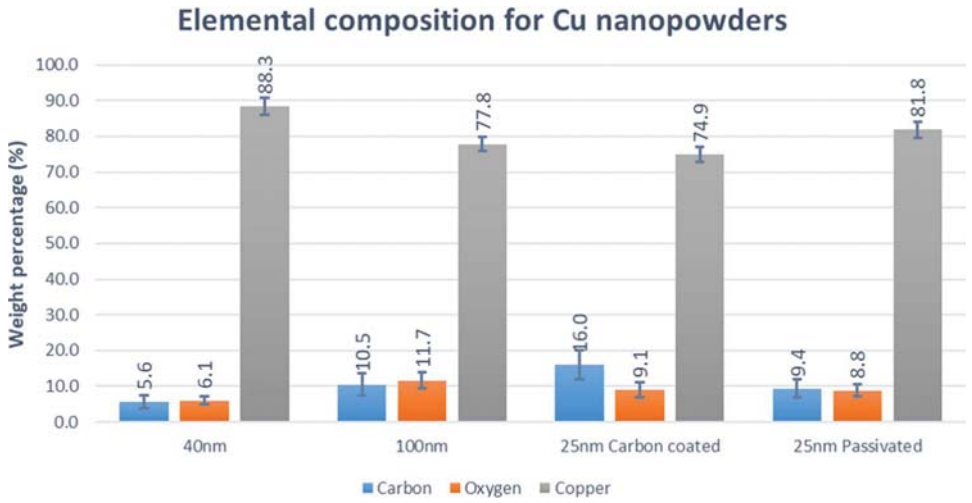

Fig. 8. Elemental composition for different nanopowder samples.

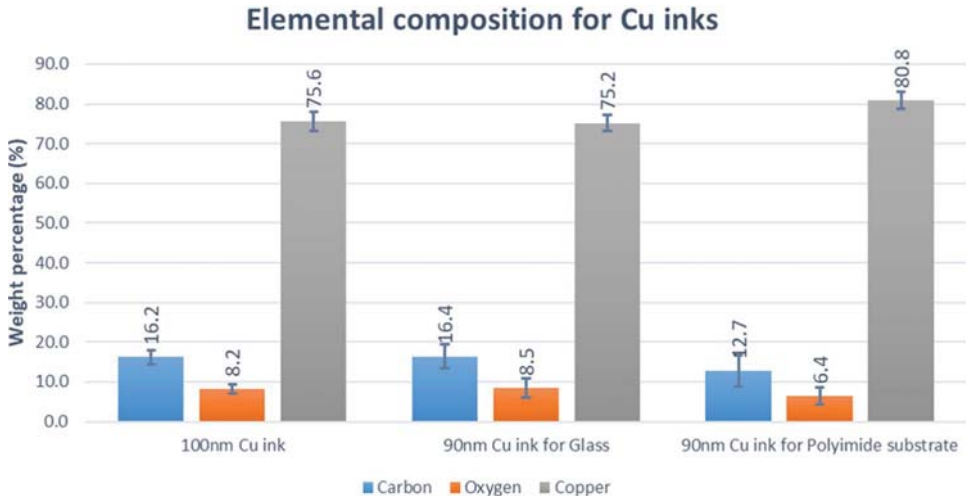

Fig. 9. Elemental composition of different nanoink samples.

SEM images of the Cu ink NPs were taken just before and just after heating to their exothermic peaks to observe how the morphology of the NPs changes around these peaks. From the SEM images above in Figs. 16 and 17, it can be seen there are clearly defined NPs in the sample when the sample is heated to just below its exothermic peak but that the particles are no longer individually identifiable and necking between the particles has started when the samples are heated to just beyond the observed exothermic peaks in the DSC. These particles are connected through their surfaces, and dumbbell-type particles can be found. The extent of sintering in 90 nm Cu ink (for glass substrate) was

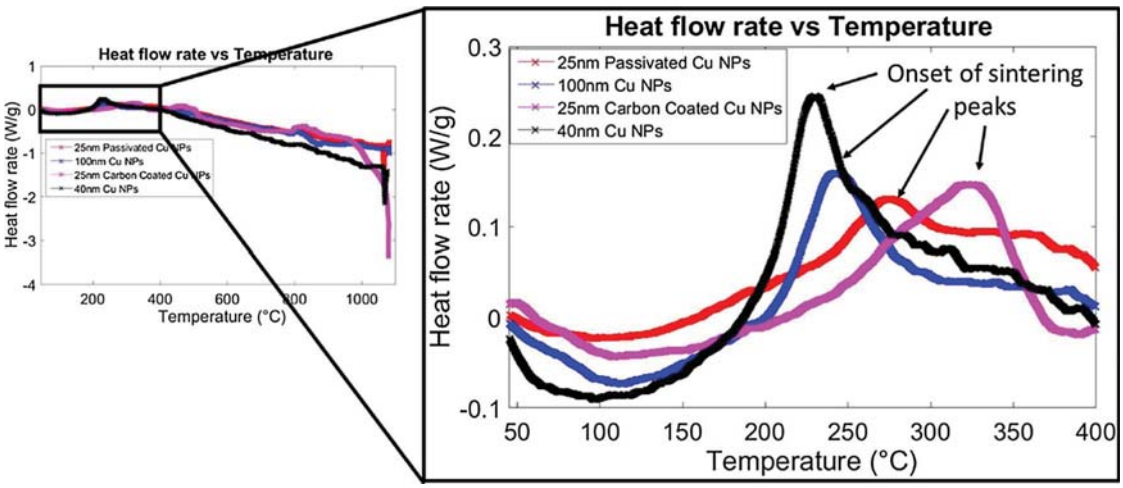

Fig. 10. Heat flow curves for powder samples between a) 45–400 °C b) 45–1085 °C.

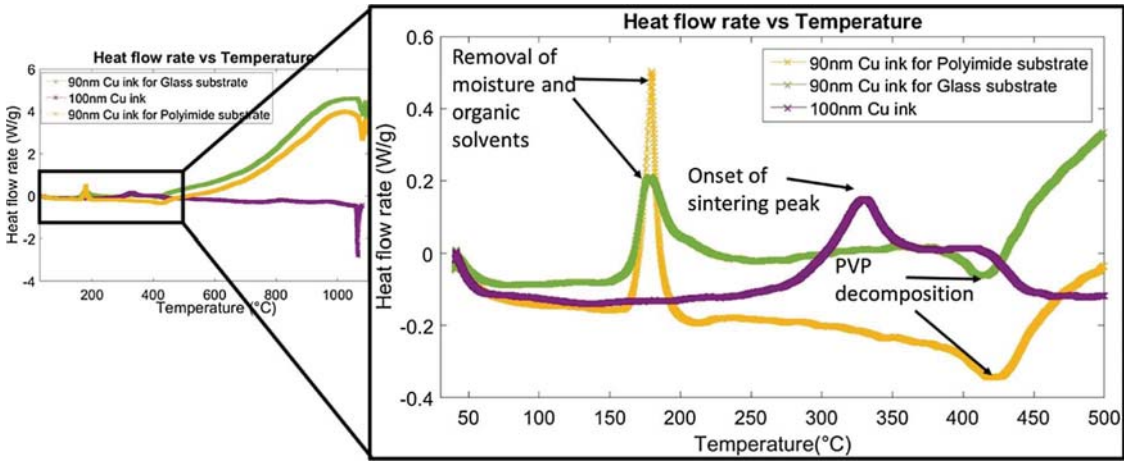

Fig. 11. Heat flow curves for the ink samples between a) 40–500 °C b) 40–1085 °C.

observed to be even higher with the particles almost fusing together once the PVP layer is decomposed. This is very similar to the morphology of an initial stage in the typical sintering process. This strengthens the hypothesis that sintering of the NPs can start at temperatures well below the melting point of the NPs. In addition, these images show clear necking of the particles rather than complete melting which is visible in Fig. 15 where the sample was heated to the bulk melting temperature. Therefore, sintering of Cu NPs starts much earlier than its melting point and its extent increases with increasing temperature [43].

3.4. Analysis of compositional changes in the Cu NPs during the sintering process

In order to help determine how the chemical composition of the NPs changes during the sintering process and to help to validate the hypothesis that the exothermic peaks observed in the DSC are due to initiation of surface sintering of the NPs during heating, the presence of oxides and other organic compounds (surfactants) on the surface of the powders and inks at different stages during the heating cycle was measured using XPS. Most samples which have been exposed to atmosphere have some adventitious carbon contamination and, thus, the surveys for the samples need to be corrected accordingly. This contamination is usually used as charge reference for XPS spectra and C-C component can be set to a value of 284.8 eV by default [44]. Quantification of the survey spectra was carried out by peak fitting of the individual peaks of the chemical species. Each peak of the species has to be fitted individually with mathematical functions or a combination of mathematical functions closely resembling the peak [45]. Another important factor that must be taken into account while estimating the concentration of a species is relative sensitivity factors for different chemical species, especially for doublet transitions such as Cu 2p in our samples [46].

Fig. 18 shows the carbon, oxygen, and Cu content in the 40 nm Cu NP sample at different stages during the heating from room temperature, to the sintering temperature (250 °C), and ultimately the melting temperature (1085 °C) of the Cu NPs. The carbon content in the sample decreases as the sample is heated which is expected. From the XPS measurements (see Supplementary Fig. S1), it is evident that oxygen in the NPs is present as metal oxide (529–530 eV). There are also trace quantities of metal carbonates (531.5–532 eV) and surface hydration can be observed at room temperature. As the temperature is increased, the metal carbonate concentration decreases due to a decrease in the carbon content. The metal oxide concentration first decreases with increasing temperature until the onset of sintering due to the reducing effects of the surface coatings exothermic reactions. However, once the surface coatings are removed, the oxygen content then starts to increase as the Cu gets oxidized at higher temperatures. In addition, the copper in the NPs was observed to have satellite peaks in between $Cu2p_{3/2}$ (933 eV) and $Cu2p_{1/2}$ (951 eV) which suggests that the Cu at room temperature is not pure Cu but an oxide of Cu, Cu_2O. Cu has high oxygen affinity and can get oxidized to Cu_2O even at low temperatures under partial oxygen pressures of 10^{-5} mm Hg [47]. As the sample is heated, the intensity of satellites tends to decrease suggesting a decrease in the Cu_2O concentration which can possibly be due to removal of surface oxide layers and this is also the reason why the metal oxide content showed decrease at 250 °C. After this, the core of the Cu starts to oxidize to CuO [47] which is substantiated by the reappearance of

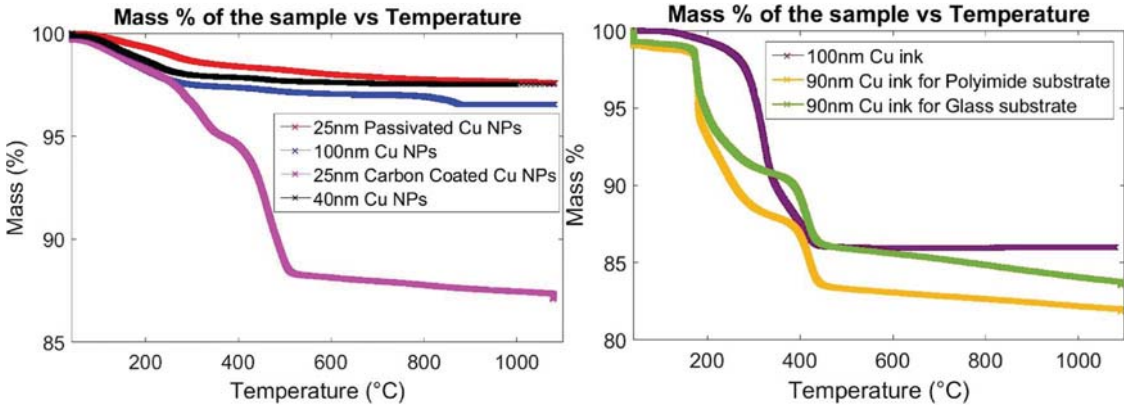

Fig. 12. Mass of the samples (in%) during the heating regime in DSC.

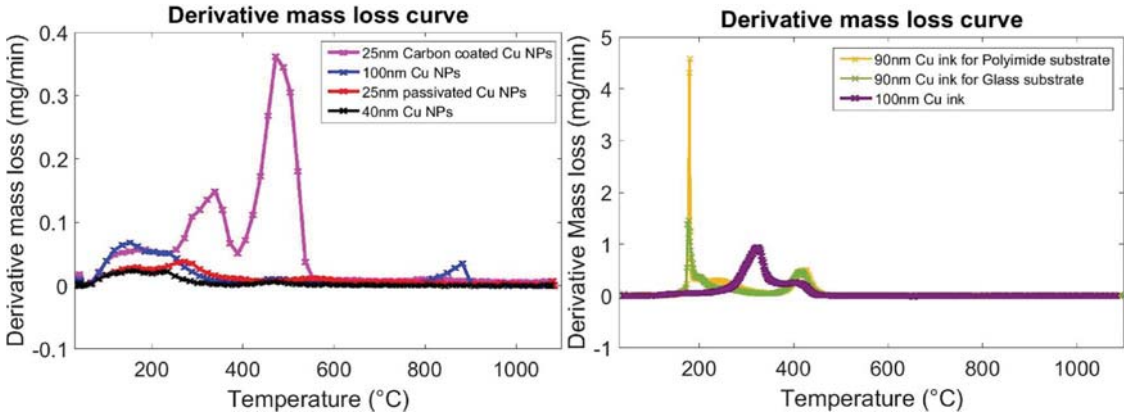

Fig. 13. Derivative mass loss of the samples a) powders and b) inks during the heating regime from 40 to 1085 °C.

satellite peaks in Cu peaks and also by an increase in metal oxide concentration at 1085 °C [48].

Fig. 19 shows the carbon, oxygen, and Cu content of the NPs in the 100 nm Cu ink at different stages during the heating: room temperature, at 300 °C (just before onset of surface sintering), at 350 °C (just after the onset of surface sintering), and finally at 1085 °C. The carbon trend in the ink sample was similar to what it was with the powder sample with the carbon content decreasing as the sample is heated (see Supplementary Fig. S2 for survey spectra). Although in the ink samples at room temperature another peak was identified at 288.6 eV which is characteristic to an organic bond O−C═O[49]. This is expected as there is likely some organic residue left even after the drying process. This peak doesn't appear at higher temperatures suggesting that the organic residue is removed when the sample is heated to high temperatures. Similarly, there are two peaks for oxygen- one at 529–530 eV and the other one at 532.5–533 eV at room temperature which have nearly the same intensity. These peaks correspond to metal oxide and organic C═O species [49]. The organic C═O peak disappears as the sample is heated indicating the removal of the organic species at higher temperatures. As the temperature is increased, the metal carbonate concentration decreases due to a decrease in the carbon content while the metal oxide concentration first decreases (till the onset of sintering) and then starts to increase at higher temperatures. Fig. 19 shows that the Cu ink sample has no satellite peaks like the powders had which suggests that the Cu in the ink sample is mostly present in the elemental Cu form. The overall trend for metallic Cu is same as that observed with the powders in that the concentration metallic Cu concentration first increases as the NPs are heated and then starts to decrease as the Cu gets oxidized more easily at the higher temperatures.

The 90 nm Cu ink (Fig. 20) shows similar behavior as shown by the 40 nm Cu NPs and 100 nm Cu ink i.e. decreasing carbon content till the organic layer is decomposed, decreasing oxygen content till the onset of sintering, and then increasing oxygen content. However, the 90 nm Cu ink sample also shows nitrogen peaks due to PVP coating of the NPs. By 450 °C, when the PVP layer is decomposed and the NPs start to sinter, both the carbon and nitrogen contents are very low and Cu concentration maximized. When the sample is subjected to higher temperatures, the carbon content on the surface of the sample is observed to increase which is likely due to the graphitization of carbon at higher temperatures in presence of Cu NPs. This phenomenon of graphitization of carbon from organic compounds such as PVP in presence of metal oxides has been reported by H. Konno et al. [50], C. Yokokawa et al. [51] and R. Sinclair et al. [52]. It suggests that these particles develop a thin carbon coating on their surface as they are heated to high temperatures.

Since XPS is a surface characterization technique, it doesn't provide much information about the bulk composition and an outer coating on the surface of the particles may provide an incorrect picture in such scenario. Thus, EDX which has penetration depths in the micrometer range depending upon the accelerating voltage and sample composition, compared to XPS which only has penetration depths of few nanometers, was also carried out to accurately identify the composition of the sample heated to 1085 °C. The weight percentages of Cu, C, N and O were found to be 68.9%, 24.5%, 1.6% and 5.0% respectively which are more consistent with what would be expected given the previous trends than the information provided by XPS surface data of this sample.

One other interesting observation for the 90 nm Cu NP inks is that when they were heated up to the melting temperature they tended to ball up much more due to surface tension effects (Fig. 21) than was observed for the NP powder samples (Fig. 15). This result could be due

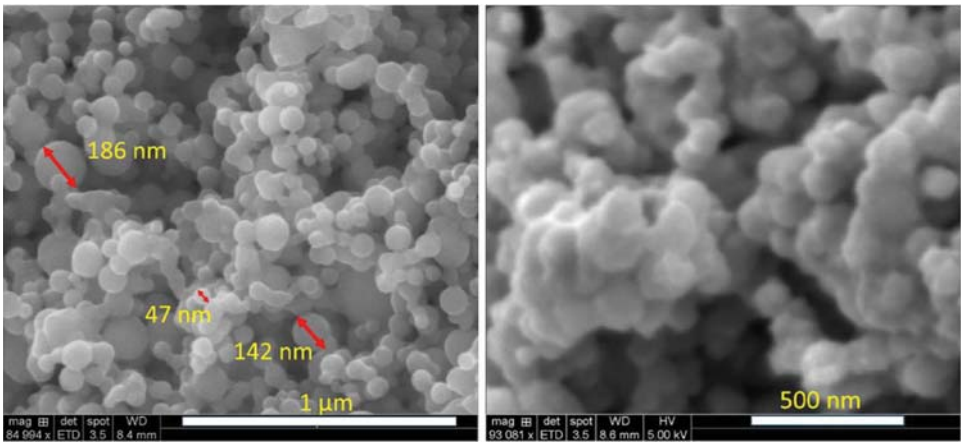

Fig. 14. Comparison of morphology of 40 nm Cu NPs sample before and after heating till 260 °C.

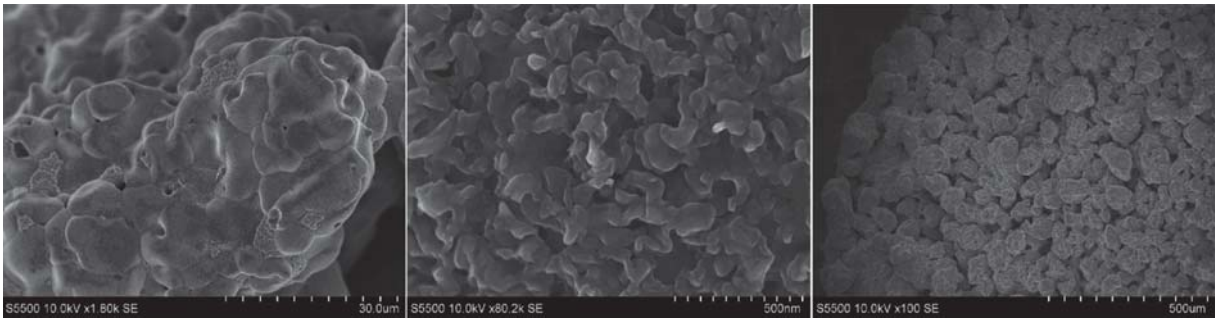

Fig. 15. a), b) and c) SEM images of the heated (till 1085 °C) 40 nm Cu NP sample.

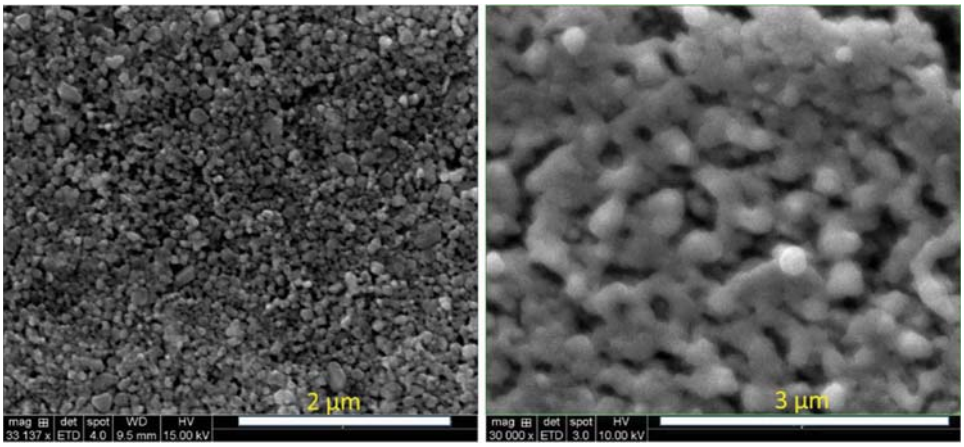

Fig. 16. Comparison of morphology of 100 nm Cu ink a) at room temperature b) heated to 350 °C.

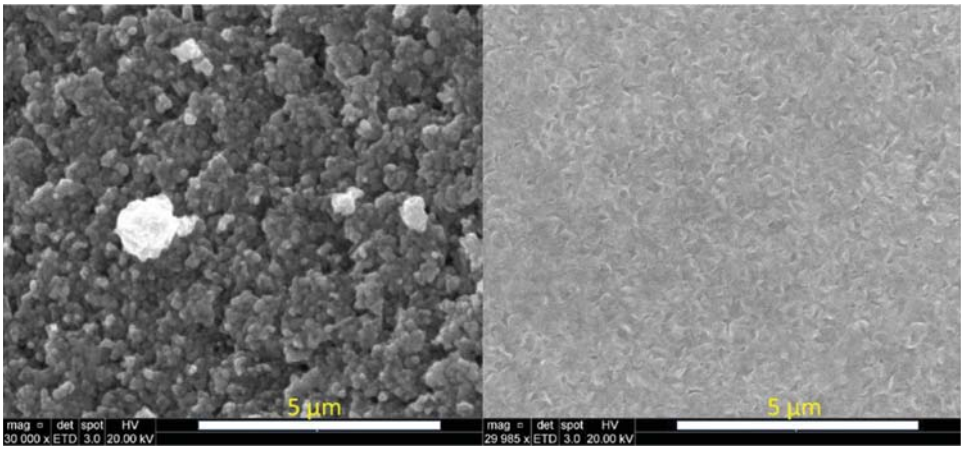

Fig. 17. Comparison of morphology of 90 nm Cu ink (with PVP coating) a) heated to 350 °C b) heated to 450 °C.

to the increased graphitic carbon observed on the surface of the 90 nm Cu NPs generated at the high temperatures which prevents complete fusion of all the NPs in the sample.

4. Discussion and conclusions

Overall, the results from this study show that how NPs are prepared can have a significant effect on the sintering properties of those NPs. Different powder samples prepared by production techniques such as electric explosion of wire and laser ablation synthesis and having different surface coatings such as carbon and passive oxide layer were studied. SEM imaging clearly showed that all the powder samples suffered with the problem of agglomeration. This makes it harder to spread a uniform layer of powder for sintering application and is highly undesirable as it degrades the properties of the final part in microscale additive manufacturing processes. Among the powders, 40 nm Cu NP sample produced by electric explosion of wire without any surface coating had the narrowest particle size distribution. Although surface coatings are intended to prevent agglomeration and oxidation of particles, both carbon coated and passivated Cu NPs had very wide size distribution and were also fibrous in appearance forming long chain like structures rather than being spherical in shape. EDX of the samples was performed to find out an estimate of the composition of different samples as a sample with high Cu content will produce parts with properties closer to that of bulk Cu compared to samples with lower Cu content. Also, this data can be used to compare the chemical changes that these samples undergo while being heated. Among the powders, 40 nm Cu NPs again had the highest Cu content with other samples

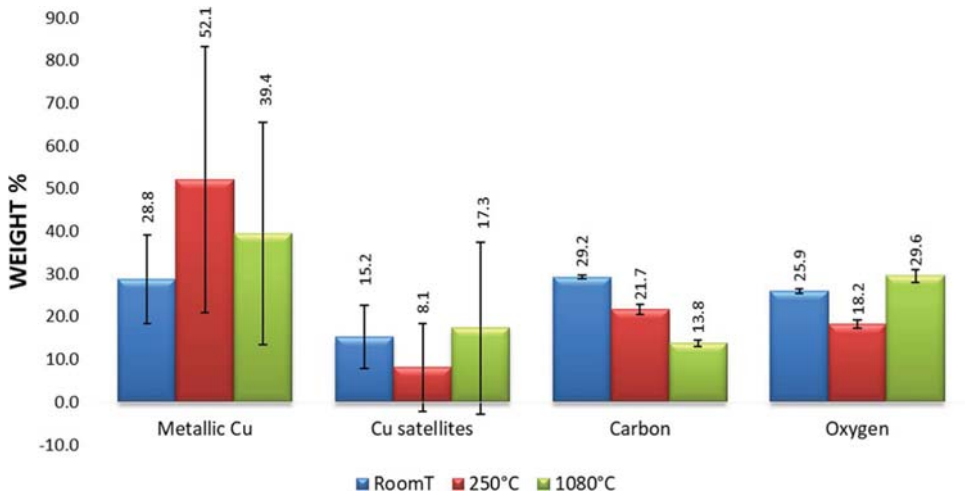

Fig. 18. Variation in concentration of different chemical species during the heating of 40 nm Cu NPs.

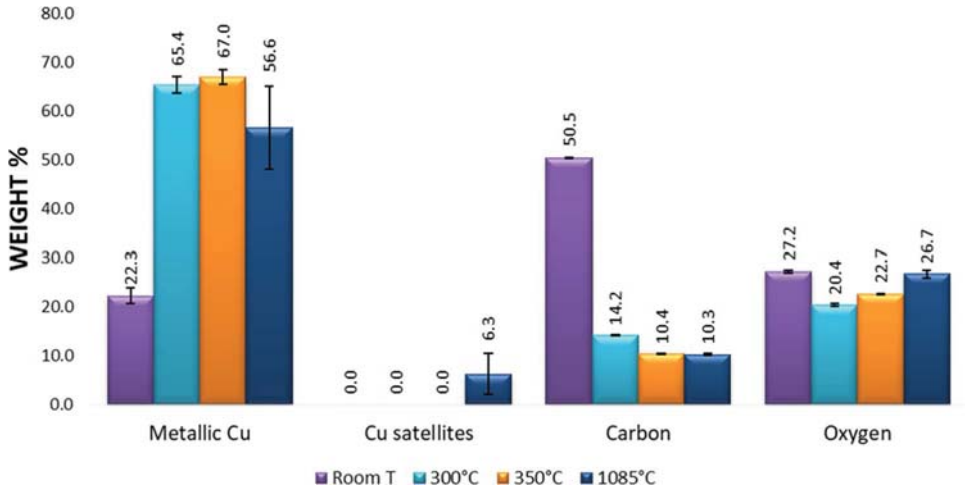

Fig. 19. Variation in concentration of different chemical species during the heating of 100 nm Cu ink.

showing expected behaviors depending upon their surface coatings. In general, the Cu NP ink samples showed much better packing, lower agglomeration, narrow size distribution, and were more uniformly shaped than particles in the powder samples.

In addition, DSC of the samples showed that all the NP samples including powders and inks can undergo surface sintering at temperatures much lower than the melting point of bulk Cu. Onset of sintering starts the earliest in the nanopowders with no coatings and then in nanopowders with protective coatings like passive oxide layer and carbon coating. The inks start to sinter at temperatures higher than nanopowders as the organic layers and residual solvents have to be decomposed before the surface sintering can begin. And thus, the 100 nm Cu ink sample which doesn't have any coating on the particles shows the onset of sintering at a lower temperature than that of 90 nm PVP coated Cu NP ink. Although the sintering onset temperature is higher in the inks compared to the powders, inks prevent any sort of

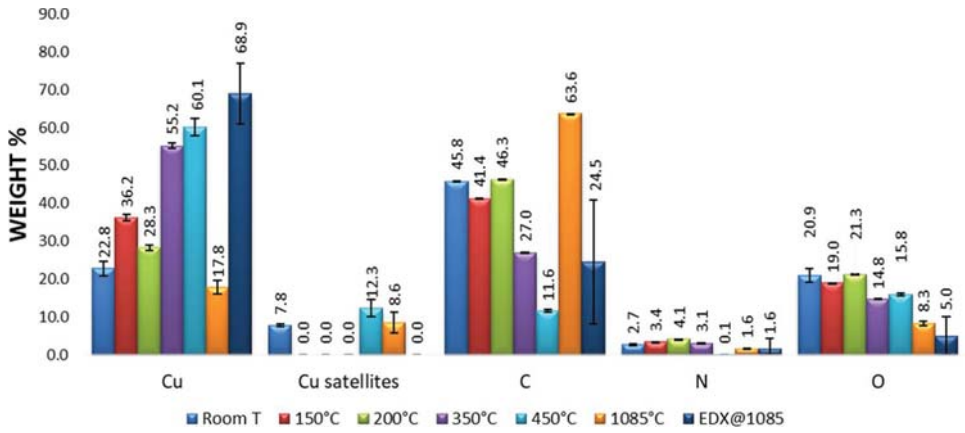

Fig. 20. Variation in concentration of different chemical species during the heating of 90 nm Cu ink (glass).

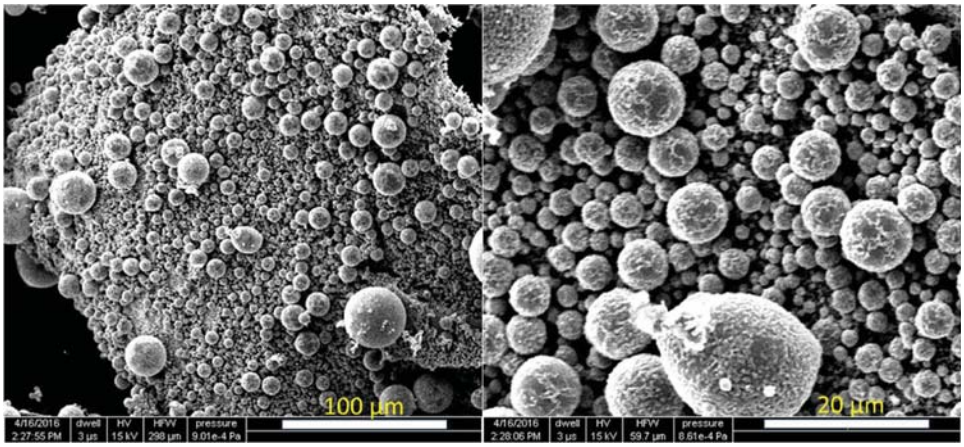

Fig. 21. a) & b) SEM images of 90 nm Cu ink (glass) sample after being heated to 1085 °C.

agglomeration of powders and maintain the packing density of the bed as they are heated. A good packing density of the sintered part is essential to achieve good fusion between particles and to get good functional properties like mechanical strength and high electrical conductivity out of the parts that are produced. Therefore, this better packing also improves the extent of sintering in inks compared to the Cu NP powders. However, the presence of PVP coating on the 90 nm Cu ink sample led to the graphitization of carbon and balling up of NPs into microparticles when the sample was heated to it melting temperature which was not observed with 100 nm Cu ink with no such coating. This suggests that organic coatings on the surface of NPs may hinder uniform melting of particles in the sample. Overall, this implies that the optimal sintering range for the Cu NP inks is between the temperatures that are high enough to decompose the polymer surface coatings but below the melting temperature of the NPs.

Acknowledgements

The authors would like to acknowledge the financial support received from NXP Semiconductors. The authors would like to thank Leo Higgins III, Ph.D. of NXP Semiconductors for his valuable inputs to the discussion on the interpretation and analysis of the experimental results. The authors would also like to thank Dr. Hugo Celio and Dr. Shouliang Zhang for assisting with the experimental setups.

Appendix A. Supplementary data

Supplementary data associated with this article can be found, in the online version, at https://doi.org/10.1016/j.addma.2018.02.008.

References

[1] M.D. Yuan Bourell, T. Diller, Thermal Conductivity Measurments of Polyamide 12, Lab. Free. Fabr. 1 (2011) 427–437.
[2] N.K. Roy, A. Yuksel, M.A. Cullinan, µ –SLS of metals: physical and thermal characterization of Cu- nanopowders, International Solid Freeform Fabrication Symposium (2015) 772–788.
[3] N.K. Roy, C.S. Foong, M.A. Cullinan, Design of a micro-scale selective laser sintering system, 2016 Annual International Solid Freeform Fabrication Symposium (2016) 1495–1508.
[4] N. Roy, A. Yuksel, M. Cullinan, Design and modeling of a microscale selective laser sintering system, ASME 2016 11th International Manufacturing Science and Engineering Conference, MSEC 2016, 2016 (V003T08A002-V003T08A002).
[5] R. Rosenberg, D.C. Edelstein, C.-K. Hu, K.P. Rodbell, Copper metallization for high performance silicon technology, Annu. Rev. Mater. Sci. 30 (1) (2000) 229–262.
[6] N.K. Roy, M.A. Cullinan, µ-SLS of Metals: Design of the powder spreader, powder bed actuators and optics for the system, Annual International Solid Freeform Fabrication Symposium (SFF), Austin, TX, August, 2015, pp. 134–155.
[7] S.a. Angayarkanni, V. Sunny, J. Philip, Effect of nanoparticle size, morphology and concentration on specific heat capacity and thermal conductivity of nanofluids, J. Nanofluids 4 (3) (2015) 302–309.
[8] Spierings, B. Adriaan, G. Levy, Comparison of density of stainless steel 316L parts produced with selective laser melting using different powder grades, Proceedings of the Annual International Solid Freeform Fabrication Symposium, Austin, TX, 2009, pp. 342–353.
[9] Bochuan Liu, et al., Investigation the Effect of Particle Size Distribution on Processing Parameters Optimisation in Selective Laser Melting Process, Additive Manufacturing Research Group, Loughborough University, 2011, pp. 227–238.
[10] M. Krantz, H. Zhang, J. Zhu, Characterization of powder flow: static and dynamic testing, Powder Technol. 194 (194) (2009) 239–245.
[11] N.K. Tolochko, S.E. Mozzharov, I.A. Yadroitsev, T. Laoui, L. Froyen, V.I. Titov, M.B. Ignatiev, Balling processes during selective laser treatment of powders, Rapid Prototyp. J. 10 (2) (2004) 78–87.
[12] A. Strondl, O. Lyckfeldt, H. Brodin, U. Ackelid, Characterization and control of powder properties for additive manufacturing, JOM 67 (3) (2015) 549–554.
[13] H.K. Rafi, D. Pal, N. Patil, T.L. Starr, B.E. Stucker, Microstructure and mechanical behavior of 17-4 precipitation hardenable steel processed by selective laser melting, J. Mater. Eng. Perform. 23 (12) (2014) 4421–4428.
[14] J.A. Slotwinski, E.J. Garboczi, Metrology needs for metal additive manufacturing powders, JOM 67 (3) (2015) 538–543.
[15] J. Lv, L. Qiu, B. Qu, Controlled growth of three morphological structures of magnesium hydroxide nanoparticles by wet precipitation method, J. Cryst. Growth 267 (3–4) (2004) 676–684.
[16] P. Wang, C. Li, H. Gong, X. Jiang, H. Wang, K. Li, Effects of synthesis conditions on the morphology of hydroxyapatite nanoparticles produced by wet chemical process, Powder Technol. 203 (2) (2010) 315–321.
[17] R. Bali, N. Razak, A. Lumb, A.T. Harris, The synthesis of metallic nanoparticles inside live plants, Proceedings of the 2006 International Conference on Nanoscience and Nanotechnology, ICONN, 2006, pp. 224–227.
[18] N.R. Jana, Z.L. Wang, T.K. Sau, T. Pal, Seed-mediated growth method to prepare cubic copper nanoparticles, Curr. Sci. 79 (9) (2000) 1367–1370.
[19] X. Song, S. Sun, W. Zhang, Z. Yin, A method for the synthesis of spherical copper nanoparticles in the organic phase, J. Colloid Interface Sci. 273 (2) (2004) 463–469.
[20] H.H. Huang, F.Q. Yan, Y.M. Kek, C.H. Chew, G.Q. Xu, W. Ji, P.S. Oh, S.H. Tang, Synthesis, characterization, and nonlinear optical properties of copper nanoparticles, Langmuir 13 (2) (1997) 172–175.
[21] D. Mott, J. Galkowski, L. Wang, J. Luo, C.J. Zhong, Synthesis of size-controlled and shaped copper nanoparticles, Langmuir 23 (10) (2007) 5740–5745.
[22] S. Panigrahi, S. Kundu, S.K. Ghosh, S. Nath, S. Praharaj, S. Basu, T. Pal, Selective one-pot synthesis of copper nanorods under surfactantless condition, Polyhedron 25 (5) (2006) 1263–1269.
[23] R. Zhou, X. Wu, X. Hao, F. Zhou, H. Li, W. Rao, Influences of surfactants on the preparation of copper nanoparticles by electron beam irradiation, Nucl. Instrum. Methods Phys. Res. Sect. B: Beam Interact. Mater. Atoms 266 (4) (2008) 599–603.
[24] V. Jankauskas, J. Padgurskas, A. Žunda, I. Prosyčevas, Research into nanoparticles obtained by electric explosion of conductive materials, Surf. Eng. Appl. Electrochem. 47 (2) (2011) 170–175.
[25] I. Lisiecki, M.P. Pileni, Synthesis of copper metallic clusters using reverse micelles as microreactors, J. Am. Chem. Soc. 115 (10) (1993) 3887–3896.
[26] E. Gaffet, G. Le Caër, Mechanical Processing for Nanomaterials, (2004).
[27] S.H. Wu, D.H. Chen, Synthesis of high-concentration Cu nanoparticles in aqueous CTAB solutions, J. Colloid Interface Sci. 273 (1) (2004) 165–169.
[28] A. Umer, S. Naveed, N. Ramzan, M.S. Rafique, M. Imran, A green method for the synthesis of copper nanoparticles using L-ascorbic acid, Matéria (Rio Janeiro) 19 (3) (2014) 197–203.
[29] D. Oleszak, P.H. Shingu, Nanocrystalline metals prepared by low energy ball milling, J. Appl. Phys. 79 (6) (1996) 2975–2980.
[30] Y. Wang, P. Chen, M. Liu, Synthesis of well-defined copper nanocubes by a one-pot solution process, Nanotechnology 17 (24) (2006) 6000–6006.
[31] R.V. Kumar, Y. Mastai, Y. Diamand, A. Gedanken, Sonochemical synthesis of nanophase indium sulfide, Mater, Mater. Chem. 11 (19) (2001) 1209–1213.
[32] M.E. Toimil Molares, V. Buschmann, D. Dobrev, R. Neumann, R. Scholz, I.U. Schuchert, J. Vetter, Single-crystalline copper nanowires produced by electrochemical deposition in polymeric ion track membranes, Adv. Mater. 13 (1) (2001)

62–65.
[33] Y. Liu, Y. Chu, Y. Zhuo, L. Dong, L. Li, M. Li, Controlled synthesis of various hollow Cu nano/microStructures via a novel reduction route, Adv. Funct. Mater. 17 (6) (2007) 933–938.
[34] B.K. Park, S. Jeong, D. Kim, J. Moon, S. Lim, J.S. Kim, Synthesis and size control of monodisperse copper nanoparticles by polyol method, J. Colloid Interface Sci. 311 (2) (2007) 417–424.
[35] W. Marine, L. Patrone, B. Luk'Yanchuk, M. Sentis, Strategy of nanocluster and nanostructure synthesis by conventional pulsed laser ablation, Appl. Surf. Sci. 154 (2000) 345–352.
[36] O. Nazarenko, a. Ilyin, Nanopowders production by electrical explosion of wires: environmental applications, Energy (2008) 19–23.
[37] N.S.F.N. Grant, Deagglomeration and Mixing of Nanoparticles, (2006), pp. 4–6.
[38] A. Sandborg, Energy Dispersive X-ray Spectrometry–eds Instrumentation & Signal DetectioN, (2015).
[39] T. Cheng, Y. Wu, H. Chen, Effects of morphology on the radiative properties of internally mixed light absorbing carbon aerosols with different aging status, Opt. Express 22 (13) (2014) 15904.
[40] N. Ichinose, Y. Ozaki, S. Kashu, Superfine Particle Technology, Springer Science & Business Media, 2012.
[41] K.-S. Moon, H. Dong, R. Maric, S. Pothukuchi, A. Hunt, Y. Li, C.P. Wong, Thermal behavior of silver nanoparticles for low-temperature interconnect applications, J. Electron. Mater. 34 (2) (2005) 168–175.
[42] Y.K. Du, P. Yang, Z.G. Mou, N.P. Hua, L. Jiang, Thermal decomposition behaviors of PVP coated on platinum nanoparticles, J. Appl. Polym. Sci. 99 (1) (2006) 23–26.
[43] I. Gibson, D. Shi, Material properties and fabrication parameters in selective laser sintering process, Rapid Prototyp. J. 3 (4) (2006) 129–136.
[44] N. Fairley, CasaXPS Manual 2.3. 15: Introduction to XPS and AES, Casa Software, 2009.
[45] T. Xps, XPS Spectra, (2013), pp. 1–77.
[46] R.S. Factors, Understanding Relative Sensitivity Factors for Doublet Transitions, (2008), pp. 1–4.
[47] A.V. Korshunov, A.P. Il'in, Oxidation of copper nanopowders on heating in air, Russ. J. Appl. Chem. 82 (7) (2009) 1164–1171.
[48] Y. Jianfeng, Z. Guisheng, H. Anming, Y.N. Zhou, Preparation of PVP coated Cu NPs and the application for low-temperature bonding, J. Mater. Chem. 21 (40) (2011) 15981.
[49] B. Vincent Crist, Handbook of Monochromatic XPS Spectra, The Elements of Native Oxides, Wiley-VCH, 2000, p. 548 ISBN 0-471-49265-5, October 2000.
[50] H. Konno, K. Fujita, H. Habazaki, M. Inagaki, Graphite formation at 1150–1200 °C from hard-carbon precursors and magnetite, Tanso 203 (203) (2002) 113–116.
[51] C. Yokokawa, K. Hosokawa, Y. Takegami, Low temperature catalytic graphitization of hard carbon, Carbon N. Y. 4 (4) (1966) 459–465.
[52] R. Sinclair, T. Itoh, R. Chin, In situ TEM studies of metal???Carbon reactions, Microsc. Microanal. 8 (4) (2002) 288–304.